Sensitivity Analysis of the Orthorhombic Design Parameters in the Artificially Biaxially Dielectric Crystal

Jason Brand and Michael A. Saville

Department of Electrical Engineering
Wright State University, Fairborn, Ohio 45435, USA
jbrand16@wright.edu, michael.saville@wright.edu

Abstract ─ A full-wave modeling and simulation analysis method is presented for performing sensitivity analysis of artificial uniaxial and biaxial crystals previously reported for study with waveguide measurement systems. Small occlusions were machined into bulk dielectric material to impose effectively biaxial material properties. Here, the primary design parameters for orthorhombic occlusions are presented. Using multivariate parameter estimation, the effective material properties are characterized in a way that is equivalent to waveguide measurement methods. The advantage in using full-wave simulation allows investigation beyond measurement and fabrication capabilities, but is still limited because of the mesh size needed to model the fine geometric sizes of the occlusions in the crystal. The analysis shows that the effects of the primary design parameters on anisotropy can achieve 2-3 dB of axial difference for the biaxially diectric crystal. Although, only the dielectric case is presented, the multivariate estimation method used to estimate the material parameters is applicable for characterizing lossy and magnetic materials.

Index Terms ─ Biaxial material, permeability, permittivity, sensitivity analysis, waveguide.

I. INTRODUCTION

Design of electromagnetic metamaterials for antenna substrates, guiding structures, and controlled scattering is challenging because the performance requirements often demand inhomogeneous and anisotropic material properties [1], [2]. Although, analysis methods using Green's functions [3] and transformational optics [4] have produced theoretical profiles for the relative permittivity and permeability, fabrications of such designs have been very limited.

Recent experimental approaches for characterizing the electromagnetic properties of bulk materials [5], [6] using rectangular waveguide measurements enable a way to systematically design biaxial materials. By placing a cubic sample in the waveguide system at four different orientations and measuring (S_{11}, S_{21}), a Newton method solution is used to estimate the material tensors from a mode-matching model of the scattering parameters.

Building upon the waveguide methods, Knisely et al. proposed a 3D printing method for making uniaxial and biaxial materials from machined bulk isotropic dielectric materials [7]. Referring to Fig. 1, the design concept is based on symmetry of the occlusions in the bulk material with respect to the primary axes of the material. A detailed summary of the underlying crystallographic theory and mathematics is nicely provided in [8]. Using an ultra-violet cured polymer material for 3D printing, [8] prints axially symmetric cubic samples that have unidirectionally air-filled vias as shown in Fig. 1. Following the mode-matching and Newton method approaches in [5], [9], Knisely et al. perform similar material characterization using waveguide measurements and full-wave simulation to validate the measurement. As the empirical approach includes measurement uncertainty, physical constraints on manufacturing, and machining uncertainty, use of full-wave modeling and simulation as a surrogate for measurement offers a way to limit the uncertainty so that the design parameters can be optimized. The simulation approach allows nearly unconstrained study of how the crystal's design parameters influence effective relative permittivity and permeability. The dominant simulation uncertainty is caused by the specific numerical method and mesh definition because of the frequency sweep.

Here, we build upon the works in [5] and [7] and present sensitivity analyses of the primary design parameters used to impose anisotropic behavior in bulk dielectric material, e.g., uniaxial ($\bar{\bar{\tau}}$ =diag[τ_A, τ_A, τ_C]) and biaxial ($\bar{\bar{\tau}}$ =diag[τ_A, τ_B, τ_C]). The approach is suitable for both measurement- and simulation-based methodologies where the designer might choose the method based on available resources or associated error sources. We demonstrate a simulation-based approach by analyzing the Knisely crystal [7] and showing how the dimensions, electric density, and pose of the vias impact the effective relative permittivity and permeability. Section II summarizes the analytic mode-matching model from [5],

Submitted On: June 4, 2015
Accepted On: August 14, 2015

[9] and how we use finite element simulation as a substitute for the measurement system in [5]. Section III presents the detailed cost function and practical considerations of the search method. Section IV presents sensitivity analysis of the artificial biaxial sample in [7], and Sections V and VI present results and conclusions.

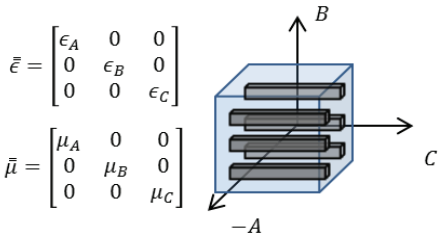

Fig. 1. Illustration of principal axes for artificial biaxial dielectric crystal of [7]. Shaded boxes denote machined vias in bulk isotropic dielectric cubic sample.

II. MODE MATCHING MODEL

Rectangular waveguide systems are convenient for biaxial material characterization because the TE_{10} mode excites only one sample axis and the biaxial region only supports odd-numbered TE_{n0} modes. Although higher-order waves are excited at the waveguide junctions, those modes evanesce and do not significantly contribute to (S_{11}, S_{21}) measurements. Hence, (S_{11}, S_{21}) are TE_{n0} (for $n = 1, 3, ...$).

Using $e^{j\omega t}$ time convention and the reduced aperture waveguide system in [5], the total electric field at the guide-sample interface nearest to measurement port 1 must satisfy:

$$A_1^+ \mathbf{e}_1^{\mathrm{wg}}(x,y)e^{-jk_{z,1}^{\mathrm{wg}}z} + \sum_{n=1}^{\infty} A_n^- \mathbf{e}_n^{\mathrm{wg}}(x,y)e^{+jk_{z,n}^{\mathrm{wg}}z} = \sum_{n=1}^{\infty}\left(B_n^- \mathbf{e}_n^{\mathrm{sa}}(x,y)e^{+jk_{z,n}^{\mathrm{sa}}z} + B_n^+ \mathbf{e}_n^{\mathrm{sa}}(x,y)e^{-jk_{z,n}^{\mathrm{sa}}z}\right), \quad (1)$$

and the total electric field at the sample-guide interface closest to measurement port 2 must satisfy:

$$\sum_{n=1}^{\infty}\left(B_n^- \mathbf{e}_n^{\mathrm{sa}}(x,y)e^{+jk_{z,n}^{\mathrm{sa}}z} + B_n^+ \mathbf{e}_n^{\mathrm{sa}}(x,y)e^{-jk_{z,n}^{\mathrm{sa}}z}\right) = \sum_{n=1}^{\infty} C_n^+ \mathbf{e}_n^{\mathrm{wg}}(x,y)e^{-jk_{z,n}^{\mathrm{wg}}z}, \quad (2)$$

where superscripts $+$ and $-$ in the amplitude coefficients A_n, B_n, C_n denote forward and backward propagation. The vector basis functions ($\mathbf{e}_n^{\mathrm{wg}}, \mathbf{e}_n^{\mathrm{sa}}$) are in general determined by two subscript indices. However, following [10], in the case of the symmetric dielectric crystal under study, only TE_{n0} modes are excited in the sample region for TE_{10} excitation. The amplitude coefficients are determined in straightforward fashion by testing each boundary equation with the electric or magnetic field basis function and solving the complete set of equations to compute $S_{11} = A_1^-/A_1^+$ and $S_{21} = C_1^+/A_1^+$.

The complete description of the mode matching equations including magnetic field boundary conditions has been presented in [5], [9] and for brevity, we refer the reader to [5] for the complete descriptions of the four boundary equations, electric field basis functions ($\mathbf{e}_n^{\mathrm{wg}}, \mathbf{e}_n^{\mathrm{sa}}$), magnetic field basis functions ($\mathbf{e}_n^{\mathrm{wg}}, \mathbf{e}_n^{\mathrm{sa}}$), propagation constants ($k_{z,n}^{\mathrm{wg}}, k_{z,n}^{\mathrm{sa}}$), and matrix algebra formulation.

The S-parameters' dependencies on $\bar{\bar{\epsilon}}_r$ and $\bar{\bar{\mu}}_r$ are utilized in a numerical search algorithm as:

$$\hat{\bar{\bar{\epsilon}}}_r, \hat{\bar{\bar{\mu}}}_r = \arg\min_{\bar{\bar{\epsilon}}_r, \bar{\bar{\mu}}_r} \|\mathbf{S}(f) - \mathbf{S}^{\mathrm{MM}}(f; \bar{\bar{\epsilon}}_r, \bar{\bar{\mu}}_r)\|_\ell, \quad (3)$$

where the specific type of ℓ-norm $\|\cdot\|_\ell$ depends on the search algorithm. As described in [5], six measurements are needed to estimate the biaxial material properties from the mode matching ($\mathbf{S}^{\mathrm{MM}}$) solutions. However, only four orientations of the sample are required when both S_{11} and S_{21} are available. Here, we use finite-element-method simulation of the physical measurement system and assemble the simulated and theoretical (mode matching) solutions as:

$$\mathbf{S} = \left[S_{11,A}, S_{21,A}, S_{11,B}, S_{11,B'}, S_{21,B'}, S_{21,C}\right]^T, \quad (4)$$

$$\mathbf{S}^{\mathrm{MM}} = \left[S_{11,A}^{\mathrm{MM}}, S_{21,A}^{\mathrm{MM}}, S_{11,B}^{\mathrm{MM}}, S_{11,B'}^{\mathrm{MM}}, S_{21,B'}^{\mathrm{MM}}, S_{21,C}^{\mathrm{MM}}\right]^T, \quad (5)$$

where subscripts A, B, B', C refer to the excitation of the sample axes as shown in Fig. 2. Clearly, measured or simulated values of $\mathbf{S}$ suffice.

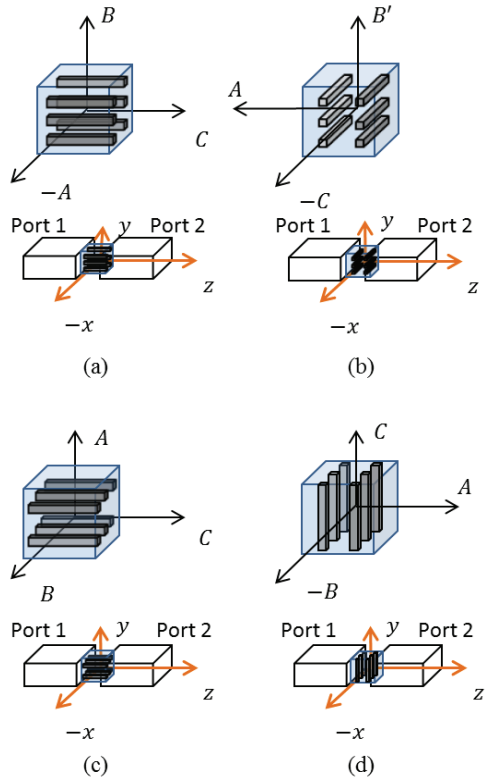

Fig. 2. Illustration of four measurement configurations needed to estimate: (a) ϵ_B, μ_A, μ_C, (b) ϵ_B, μ_A, μ_C, (c) ϵ_A, μ_B, μ_C, and (d) ϵ_C, μ_A, μ_B using reduced aperture waveguide system [5].

III. MATERIAL PROPERTY CHARACTERIZATION

The solution to Equation (3) can be determined directly, but is computationally expensive. Alternatively, we use the iterative approach in [5] where,

$$\hat{\epsilon}_B, \hat{\mu}_A, \hat{\mu}_C = \arg\min \left\| \begin{bmatrix} S_{11,B} \\ S_{21,B} \\ S_{21,B'} \end{bmatrix} - \begin{bmatrix} S_{11,B}^{\mathrm{MM}}(\epsilon_B, \mu_C, \mu_A) \\ S_{21,B}^{\mathrm{MM}}(\epsilon_B, \mu_C, \mu_A) \\ S_{21,B'}^{\mathrm{MM}}(\epsilon_B, \mu_C, \mu_A) \end{bmatrix} \right\|_\ell, \quad (6)$$

$$\hat{\epsilon}_A, \hat{\mu}_B = \arg\min \left\| \begin{bmatrix} S_{11,A} \\ S_{21,A} \end{bmatrix} - \begin{bmatrix} S_{11,A}^{\mathrm{MM}}(\epsilon_A, \mu_B, \hat{\mu}_C) \\ S_{21,A}^{\mathrm{MM}}(\epsilon_A, \mu_B, \hat{\mu}_C) \end{bmatrix} \right\|_\ell, \quad (7)$$

$$\hat{\epsilon}_C = \arg\min \left\| [S_{21,C}] - \left[S_{21,A}^{\mathrm{MM}}(\epsilon_C, \hat{\mu}_A, \hat{\mu}_B) \right] \right\|_\ell. \quad (8)$$

Equations (6) to (8) are solved using non-linear optimization [11, chap. 4], [12], e.g., Newton method uses the ℓ_1 norm and gradient descent uses the ℓ_2 norm. We observed a more stable solution using the ℓ_1 norm. Also, in each case, the cost function is often decomposed into real and imaginary components.

For example, the cost function in Equation (8), which uses the sample orientation of Fig. 2 (d) and estimates of permeability from Equations (6) and (7), would typically be expressed explicitly in terms of real and imaginary parts as:

$$\hat{\epsilon}_{C,re}, \hat{\epsilon}_{C,im} = \arg\min \left\| \begin{bmatrix} \text{real } S_{11,A} \\ \text{imag } S_{21,A} \end{bmatrix} - \begin{bmatrix} \text{real } S_{11,A}^{\mathrm{MM}}(\epsilon_C, \hat{\mu}_A, \hat{\mu}_B) \\ \text{imag } S_{21,A}^{\mathrm{MM}}(\epsilon_C, \hat{\mu}_A, \hat{\mu}_B) \end{bmatrix} \right\|_\ell. \quad (9)$$

However, these search methods are sensitive to the initial search point. The cost functions represented by Equations (6) to (8) are highly oscillatory and have many local minima and maxima. As the contrast between the air-filled waveguide and sample-filled test regions increases, the search volume increases and the iterative search algorithms can take a very long time.

Hence, we have found it best to constrain the search according to physical reasoning. For the material models $\epsilon_{re} - j\epsilon_{im}$, $\mu_{re} - j\mu_{im}$ with dielectric, non-magnetic, and lossless conditions $\epsilon_{re} \geq 1.0$, $\mu_{re} = 1.0$, and $\epsilon_{im}, \mu_{re} = 0.0$.

Therefore, Equations (6), (7), (8) represent six, four and two simultaneous equations, respectively. We use non-linear constrained least squares because it is very fast and straightforward to implement. In this study, the specific constraints are:

$$1.0 \geq \epsilon_{re} \geq \epsilon_r \in [2.8, 5.6], \quad (10)$$

$$0.0 \leq \epsilon_{im} \leq 0.1, \quad (11)$$

$$1.0 \leq \mu_{re} \leq 1.1, \quad (12)$$

$$0.0 \geq \mu_{im} \leq 0.1. \quad (13)$$

The parameter estimation process is still supervised because there are many local minima. Table 1 lists the algorithm used to extract all 6 complex-valued material properties. In addition, the tolerance (TOL) determines when the result has not changed significantly and when the residual of the cost function is sufficiently small. However, when using a single mesh to simulate the *S*-parameters, the numerical error increases with frequency. Therefore, the supervised process allows the supervisor to accept a larger residual error. We observed residuals of the order of 0.01 for the upper range of frequencies.

Table 1: Supervised search algorithm

Input	$\mathbf{S}$, $\mathbf{S}^{\mathrm{MM}}$ from Eqs. (4), (5), TOL=*0.001*, Constraint Equations (10) to (13)
Output	$\bar{\bar{\epsilon}}_r, \bar{\bar{\mu}}_r$ for all frequencies
FOR	q-th frequency, f_q
Step 1	Estimate $\epsilon_B(f_q),\ \mu_A(f_q),\ \mu_C(f_q)$
initialize $\hat{\epsilon}_B(f_q), \hat{\mu}_A(f_q), \hat{\mu}_C(f_q)$ in Eqs. (10) to (13) IF $q > 1$, initialize with $(q-1)$ estimates	
WHILE Equations (10) to (13) are unsatisfied $[\hat{\epsilon}_B(f_q), \hat{\mu}_A(f_q), \hat{\mu}_C(f_q)]$ from Equation (6) $r = \left\| \mathbf{S}(f_q) - \mathbf{S}^{\mathrm{MM}}(f_q; \hat{\bar{\bar{\epsilon}}}_r(f_q), \hat{\bar{\bar{\mu}}}_r(f_q)) \right\|_1$	
IF $r <$ TOL GOTO *Step 2*, ELSE repeat *Step 1*	
Step 2	Estimate $\epsilon_A(f_q),\ \mu_B(f_q)$
initialize $\hat{\mu}_C(f_q)$ from *Step 1* initialize $\hat{\epsilon}_B(f_q), \hat{\mu}_A(f_q)$ in Equations (10) to (11) IF $q > 1$, initialize with $(q-1)$ estimates	
WHILE Equations (10) to (13) are unsatisfied $[\hat{\epsilon}_A(f_q), \hat{\mu}_B(f_q)]$ from Equation (7) $r = \left\| \mathbf{S}(f_q) - \mathbf{S}^{\mathrm{MM}}(f_q; \hat{\bar{\bar{\epsilon}}}_r(f_q), \hat{\bar{\bar{\mu}}}_r(f_q)) \right\|_1$	
IF $r <$ TOL GOTO *Step 3*, ELSE repeat *Step 2*	
Step 3	Estimate $\epsilon_C(f_q)$
initialize $\hat{\mu}_A(f_q),\ \hat{\mu}_B(f_q)$ from *Step 1* and *Step 2* initialize $\hat{\epsilon}_C(f_q)$ in Equations (10) to (11) IF $q > 1$, initialize with $(q-1)$ estimates	
WHILE Equations (10) to (13) are unsatisfied $[\hat{\epsilon}_C(f_q)]$ from Equation (8) $r = \left\| \mathbf{S}(f_q) - \mathbf{S}^{\mathrm{MM}}(f_q; \hat{\bar{\bar{\epsilon}}}_r(f_q), \hat{\bar{\bar{\mu}}}_r(f_q)) \right\|_1$	
IF $r <$ TOL next frequency, ELSE repeat *Step 3*	

IV. BIAXIAL MATERIAL FROM MACHINED BULK ISOTROPIC MATERIAL

We perform the analysis by analyzing simulated biaxial properties of the artificial material proposed by [7], where rectangular vias are unidirectional along the *C*-axis (Fig. 3 (a)). Figure 3 (b) illustrates the cross-sectional dimensions of a via (δ_A, δ_B) and its pose angle (ψ). Additionally, Fig. 3 (c) depicts the uniform array of vias with $N_A = 4$ along the *A* axis and $N_B = 8$ along the *B* axis and sized to fit within the short dimension of WR90 waveguide.

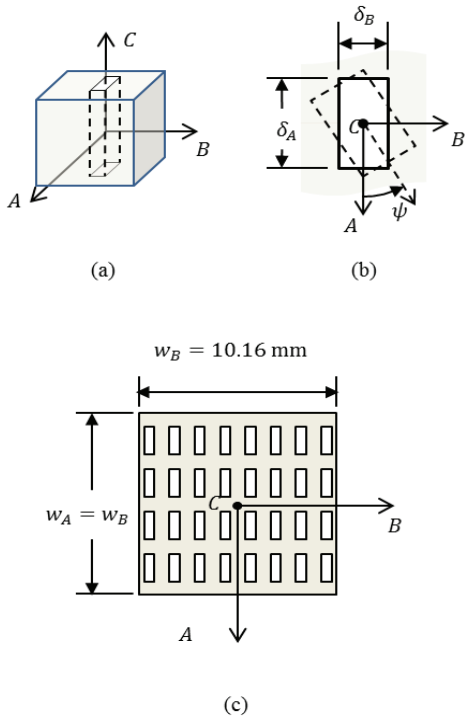

Fig. 3. Illustration of symmetric crystal design [7]. (a) Cubic sample showing single via (dashed lines) relative to principal axes. (b) Cross-sectional view of orthorhombic via showing dimensions along *A* and *B* axes and pose angle. (c) Biaxial design similar to [7] with $N_A = 4, N_B = 8,\ \delta_A = 1.53$ mm, $\delta_B = 0.51$ mm, and $\psi = 0$ deg.

A. Simulation parameters

Then, we simulate the *S*-parameters for the variety of design variables listed in Table 2 and observe how the particular combination of via pose, dimension and number affect the relative material properties. The vias are air-filled, and although we could consider vias filled with other materials, we elect a pragmatic set of material properties which are easily fabricated with 3D printing and typical of printing materials. To assist in comparing to other works, we define the air ratio as the ratio of the cross-section of air (via) to the cross-section of dielectric material with respect to each axis as:

$$\rho_A = \delta_B N_B/(L - \delta_B N_B), \quad (14)$$

$$\rho_B = \delta_A N_A/(L - \delta_A N_A), \quad (15)$$

$$\rho_C = \delta_A N_A \delta_B N_B/(L^2 - \delta_A N_A \delta_B N_B), \quad (16)$$

where the edge length *L* of the cubic sample is sized to fit inside the cubic waveguide section of the reduced-aperture system (Fig. 2) [5]. We chose that system rather than the transition guide in [7] because it is smaller in size and poses a lower computational burden. It also has an exact mode-matching solution needed for root finding in Equations (6) to (8). The bulk material is assumed to be lossless, homogeneous and the guide walls are perfectly electrically conducting waveguide walls. We simulate S_{11} and S_{21} for each orientation in Fig. 2 and de-embed to the sample planes for comparison with the mode matching solution. Then, we follow the procedure described in Section III where we use non-linear least squares with the constraints in Equations (10) to (13).

In summary, each configuration of Table 2 required four simulations at nine frequencies for a total of 864 simulations for the uniaxial case without via rotation, and another 864 simulations for the biaxial case without via rotation. Simulations were completed on a Unix server hosting dual, 3.3 GHz, six-core Xeon X5680 processors and 15GB RAM. In the cases of non-zero pose angle, only 144 simulations were needed.

Table 2: Study parameters for artificial uni/biaxial material

Design Constraints	
Type	Uniaxial
Bulk permittivity	$\epsilon_r \in [2.8, 5.6]$
Bulk permeability	$\mu_r = 1.0$
Via size	$\delta \in [1.0 : 0.5 : 5.0]$ mm
Lattice size	$N = 2,3,\ldots,7$
Pose angle	$(\delta = 1.0$ mm$, N = 6)$, $\psi = 0,15,\ldots,45$ deg
Air ratio	$0.04 < \rho_C < 31.00$
Type	Biaxial
Bulk permittivity	$\epsilon_r = 2.86$
Bulk permeability	$\mu_r = 1.0$
Via size	$\delta_A = 1.53$ mm, $\delta_B = 0.51$ mm,
Lattice size	$N_A \in [2,3,\ldots,6]$, $N_B \in [2,4,\ldots,10]$
Pose angle	$\psi = 0$ deg
Air ratio *A* axis	$0.11 < \rho_A < 1.00$
Air ratio *B* axis	$0.33 < \rho_B < 1.29$
Air ratio *C* axis	$0.03 < \rho_C < 0.83$

B. Comments on finite-element modeling

In this work, simulations are performed using the finite element method as implemented in COMSOL version 4.4 [13]. To increase efficiency, the mesh was sized according to the middle frequency of the nine-point sweep (i.e., 8.0 to 10.0 GHz in 0.50 GHz steps). Typical mesh density is of the order of 10 samples per guided wavelength (λ_g). However, from Table 2, the sizes of the vias are much smaller than $\lambda_g/50$ which could cause numerical instability and unacceptable numerical error.

Hence, we first meshed the sample region exactly the same as the most densely occluded configuration of Table 2. The mesh in the sample region was of the order of $\lambda_g/100$, while the meshes in the WR90 waveguide sections were of the order of $\lambda_g/8$ using a tetrahedral mesh. Then, we verified that the numerical error of the

S-parameters did not exceed 0.01 using an air-filled sample region. In other words, we followed the procedure outlined in Section III for an isotropic air-filled sample and verified that the extracted relative material tensors were identity tensors.

We also considered the length of the WR90 waveguide sections. Under the premise that only TE_{10} modes will propagate back to Port 1 and forward to Port 2 because the high-order modes will evanesce, we studied lengths of WR90 ranging from 0.33 λ_g to 1.00 λ_g. The *S*-parameters had a larger error for the shorter length, but the relative error of the *S*-parameter magnitude was of the order of 0.01. The increased error suggests weakly evanescent modes still affect the *S*-parameter calculation which is based on a pure TE_{10} mode. Hence, we continued to use waveguide sections with lengths of the order of 1.0 λ_g.

Lastly, should one choose to check how the effective material property compares to a bulk material that exhibits the same biaxial properties, it is necessary to simulate the anisotropic bulk material. Clearly, the bulk material eliminates the need for a finely detailed mesh in the sample region. However, the different discretization approaches can cause numerical differences. Hence, the mesh for the anisotropic bulk material can be the same as the mesh for the machined isotropic bulk material. There are different ways to define the anisotropy. First, the material can be defined for the sample region which requires the modeler to carefully select all of the subdomain elements. This approach can be tedious. An alternative approach is to redefine the constitutive relations in the sample region and assume a completely air-filled region. We elected the latter approach which significantly reduced the time needed to build the dozens of geometric models listed in Table 2 and eliminated accidental exclusion of a tetrahedron in the sample region.

V. RESULTS

A. Effects on uniaxial design

Referring to Table 2, we modeled 23 combinations of square via size and number to provide air ratio values ranging from 0.04 to 31. Additionally, vias were placed symmetrically and uniformly in the *A*-*B* plane. Estimated material parameter values had imaginary components of 0.00 ± 0.05 and μ_{re} equaled 1.00 ± 0.05 and agreed with the lossless and non-magnetic constraints. For this reason, we only show the results of real($\bar{\bar{\epsilon}}$).

Figure 3 shows the effective relative permittivity versus frequency for both bulk dielectrics and three levels of air ratio along the *C* axis ($\rho_{C,1} = 0.03$, $\rho_{C,2} = 0.93, \rho_{C,3} = 31.00$). As expected, the effective relative permittivities tend toward 1.0 for large air-to-dielectric ratios, toward the bulk dielectric value for small ratios and toward $(\epsilon_r + 1)/2$ when the air and dielectric cross-sections are nearly equal.

We define the normalized effective relative permittivity as $\tilde{\epsilon} = (\hat{\epsilon} - 1)/(\epsilon_r - 1)$ to compare effects of different design parameters and present results for the square vias at 10.0 GHz. Figure 4 only shows curves of $\tilde{\epsilon}_C$ because the curves for $\tilde{\epsilon}_A$ have similar trends. We also show $\tilde{\epsilon}_C$ as calculated from the dimensions used in [7] (Fig. 4 dashed lines with ⊗).

To determine the range of ρ_C that results in the maximum axial difference, we graph the normalized axial difference $|\epsilon_A - \epsilon_C|/(\epsilon_r - 1)$ in Fig. 5. As there are multiple design combinations that result in the same value of ρ_C, dark solid and dashed lines denote the averages. The results show that the square via design can achieve 2-3 dB axial difference for values of ρ that span 1 to 2 orders of magnitude.

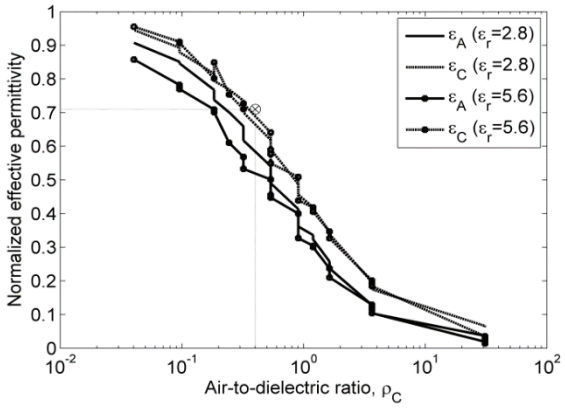

Fig. 4. Uniaxial normalized effective relative permittivity versus air-to-dielectric ratio along *C* axis. Dashed line and marker highlight $\tilde{\epsilon}_C$ from [7].

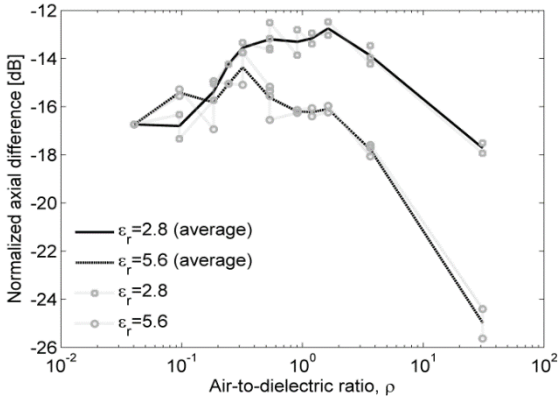

Fig. 5. Uniaxial, axial difference of effective relative permittivity versus air-to-dielectric ratio along the *C* axis at 10.0GHz.

B. Effects on biaxial design

Figure 6 shows the effective relative permittivity versus frequency for the biaxial design parameters in

Table 2 and shows distinct anisotropy for $\rho = 0.83$. The normalized axial differences $\tilde{\epsilon}_A$ and $\tilde{\epsilon}_B$ are shown in Fig. 7. The trend for $\tilde{\epsilon}_A$ is similar to the uniaxial behavior seen in Fig. 5, achieving 2-3 dB axial difference, but $\tilde{\epsilon}_B$ appears to be more sensitive to increasing air-to-dielectric ratio.

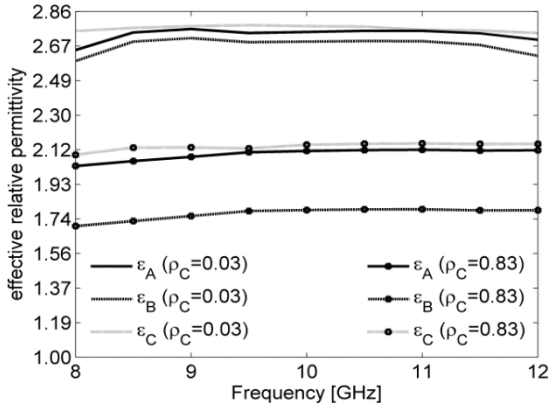

Fig. 6. Biaxial effective relative permittivity versus frequency for two different levels of air ratio ($\rho_C = 0.03$ and $\rho_C = 0.83$).

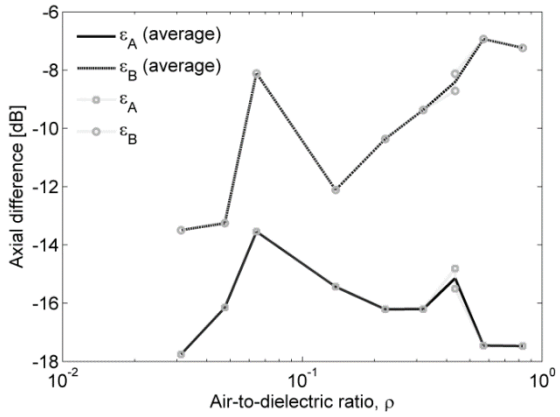

Fig. 7. Biaxial, axial difference versus air-to-dielectric ratio along *C* axis at 10.0 GHz.

VI. CONCLUSION

A detailed analysis method is presented for studying the sensitivity of the effective biaxial dielectric material properties as imposed by the primary design parameters of a recently reported orthorhombic dielectric crystal design. Using a well-known mode-matching model for characterizing the effective relative permittivity and permeability tensors, we demonstrate the process and show how the air-filled orthorhombic occlusions in bulk dielectric material can achieve a 3-dB axial difference. The analysis method is suitable for both measurement- and simulated-based methodologies and for lossy and magnetic materials.

ACKNOWLEDGMENT

The authors thank Dr. Jeffrey Allen and Dr. Monica Allen of the Air Force Research Laboratory, and Ms. Karen Bocko of S4, Inc. for supporting this work.

REFERENCES

[1] J. B. Pendry, D. Schurig, and D. R. Smith, "Controlling electromagnetic fields," *Science*, vol. 312, no. 5781, pp. 1780-1782, 2006.

[2] H. Tao, J. J. Amsden, A. C. Strikwerda, K. Fan, D. L. Kaplan, X. Zhang, R. D. Averitt, and F. G. Omenetto, "Metamaterial silk composites at terahertz frequencies," *Advanced Materials*, vol. 22, no. 32, pp. 3527-3531, Feb. 2010.

[3] M. Havrilla, "Scalar potential formulation for a uniaxial inhomogeneous medium," in *Radio Science Meeting (USNC-URSI NRSM), 2014 United States National Committee of URSI*, pp. 1-1, Jan. 2014.

[4] N. Kundtz, D. Smith, and J. Pendry, "Electromagnetic design with transformation optics," *Proceedings of the IEEE*, vol. 99, no. 10, pp. 1622-1633, Oct. 2011.

[5] B. Crowgey, O. Tuncer, J. Tang, E. Rothwell, B. Shanker, L. Kempel, and M. Havrilla, "Characterization of biaxial anisotropic material using a reduced aperture waveguide," *Instrumentation and Measurement, IEEE Transactions on*, vol. 62, no. 10, pp. 2739-2750, Oct. 2013.

[6] N. G. Rogers, M. J. Havrilla, M. W. Hyde, and A. E. Bogle, "Nondestructive electromagnetic material characterization of uniaxial media using a two-flanged rectangular-waveguide technique," *Radio Science Meeting (Joint with AP-S Symposium), 2014 USNC-URSI*, pp. 20, July 6-11, 2014.

[7] A. Knisely, M. Havrilla, P. Collins, M. Hyde, A. Bogle, J. Allen, and E. Rothwell, "Biaxial anisotropic material characterization using rectangular to square waveguide," in *36th Annual Antenna Measurement & Techniques Association Symposium*, Oct. 2014.

[8] A. Knisely, *Biaxial Anisotropic Material Development and Characterization Using Rectangular to Square Waveguide*, M.S. Thesis, Air Force Institute of Technology, Mar. 2015.

[9] J. Tang, J. B. Crowgey, O. Tuncer, E. Rothwell, B. Shanker, L. Kempel, and M. Havrilla, "Characterization of biaxial materials using a partially-filled rectangular waveguide," *Applied Computational Electromagnetics Society Journal*, vol. 28, no. 12, pp. 1134-1144, Dec. 2013.

[10] V. Dmitriev, "Tables of the second rank constitutive tensors for linear homogeneous media described by the point magnetic groups of symmetry," *Progress in Electromagnetics Research*, vol. 28, pp. 43-95, 2000.

[11] J. K. Au, *An Ab Initio Approach to the Inverse*

Problem Based Design of Photonic Bandgap Devices, Ph.D. dissertation, California Institute of Technology, 2007. [Online]. Available: http://resolver.caltech.edu/CaltechETD:etd-05242007-160527.

[12] L. Sorber, M. V. Barel, and L. D. Lathauwer, "Unconstrained optimization of real functions in complex variables," *Optimization, SIAM Journal on*, vol. 22, no. 3, pp. 879-898, 2012.

[13] COMSOL Multiphysics 4.4. url: www.comsol.com.

[14] A. Knisely, M. Havrilla, and M. Hyde, "Material characterization uncertainty analysis for rectangular to square waveguide," in *2015 IEEE AP-S Symposium on Antennas and Propagation and URSI CNC/USNC Joint Meeting*, July 2015.

Jason Brand completed the B.S.E.E. and M.S.E.E. degrees at Wright State University in 2013 and 2015, respectively. He is a veteran of the United States Air Force and is currently with Northrup Grumman.

Michael A. Saville received the B.S.E.E., M.S.E.E. and Ph.D. degrees from Texas A&M University in 1997, the Air Force Institute of Technology in 2000, and the University of Illinois at Urbana-Champaign in 2006, respectively. He is currently an Assistant Professor at Wright State University.